Bulletin of Geography. Physical Geography Series, No. 29 (2025): 85–104
http://doi.org/10.12775/bgeo-2025-0011

Rayleigh-wave group-velocity maps of Thailand, Myanmar and Malaysia derived from Ambient Noise Tomography with parameter testing

Kasemsak Saetang[1a]*, **Wilaiwan Srisawat**[2b]

[1]Nakhon Si Thammarat Rajabhat University, Faculty of Education, Program in Physics,
Nakhon Si Thammarat, Thailand

[2]Watthapho Municipal School, Science and Technology Unit, Nakhon Si Thammarat, Thailand

*E-mail: light2529@gmail.com

[a] https://orcid.org/0000-0001-8247-9884, [b] https://orcid.org/0000-0003-2590-7883

Abstract. Ambient Noise Tomography (ANT) was employed using data from 52 seismic stations – 26 from the Thai Meteorological Network and 26 from surrounding networks, collected over a specific time frame. Dispersion curves were systematically stacked over three-month intervals to mitigate seasonal variations, accepting only those with SNR ≥ 2 and SD ≤ 0.1 km·s^{-1}. Rigorous parameter tests validated the methodology, which was found to be particularly appropriate for seismic investigations in the geologically complex regions of Thailand, the Malaysia Peninsula and the Thailand Peninsula, emphasising the Central Basin. The study generated detailed Rayleigh-wave group-velocity maps, revealing significant lateral variations in seismic velocities. High-velocity zones were predominantly associated with the Shan-Thai Terrane, whereas low-velocity areas were observed in Northern Thailand, the West-Burma Terrane and the Khorat Plateau. Comparative analysis with existing studies corroborates the validity of our methodology. The results provide a detailed characterisation of the seismic landscape, encompassing structures from the upper crust to deeper features such as the mid-crustal Conrad discontinuity. This study has wider implications for earthquake preparedness and resource exploration, while also acknowledging specific limitations associated with data constraints. Overall, this study affirms the effectiveness of ANT as an invaluable tool for seismic research in regions with intricate geological histories and active tectonic settings.

Key words:
Indo-China Terrane,
Parameter Tests,
Peninsula Malaysia,
Peninsula Thailand,
Shan-Thai Terrane,
West-Burma Terrane

Introduction

Thailand, bordered by Cambodia, Laos, Malaysia and Myanmar, is a seismically active region with 15 major fault zones contributing to its complex seismic landscape (Kosuwan et al. 2018). Notable among these are the Mae Ping and Three Pagodas fault zones, which feature North-west–South-east (NW-SE) directions with left-lateral and right-lateral strike slips (Searle and Morley 2011). Additionally, the Sagaing fault zone in Burma connects to the Mae Ping fault zone and exhibits a right-lateral strike-slip. The southern region is characterised by the Khlong Marui and Ranong fault zones, both with left-lateral strike slips, while the northern part of Thailand hosts complex fault systems with varying directions and lateral movements. Recent GPS measurements have also indicated active right-lateral movements in the Ailao Shan-Red River shear zone. These intricate fault systems are crucial for understanding seismic wave propagation and significantly contribute to the seismic hazards in Thailand and its surrounding regions (see Fig. 1 for geological structures).

Seismic hazards in Thailand are primarily caused by the movement of tectonic plates along fault zones.

There are seismic hazards in the northern, southern and western regions of Thailand. During the period from 2007 to 2017, the Seismological Bureau of the Thai Meteorological Department reported a total of over 2,000 earthquakes in Thailand (Thai Meteorological Department 2018). These earthquakes exhibit a wide range of magnitudes, and, despite the majority being minor and remaining undetected by the general populace, there exists the potential for larger and more destructive quakes to occur in the future.

Although a multitude of studies have investigated the seismic characteristics of Thailand and adjacent regions, the majority have concentrated on conventional seismological methodologies or have been confined to particular fault zones (Searle and Morley 2011; Kosuwan et al. 2018). Furthermore, existing research has often concentrated on the Shan-Thai and Indo-China Terranes individually, without providing a comprehensive, high-resolution map of crustal structures across these terranes (Stokes et al. 1996; Cobbing 2011). This leaves a critical gap in our understanding of the subsurface geology at the intersection of these terranes and its implications for seismic activity. Our study seeks to address this research gap by employing the ANT to develop comprehensive Rayleigh-wave group-velocity maps for Thailand and its surrounding regions. Thereby, we provide a more detailed understanding of the crustal heterogeneity across these terranes, thus contributing to the seismic hazard assessment and geophysical understanding of the region.

Geological studies have been conducted to better understand the seismic hazard in Thailand and to investigate various aspects of the geology of this country. Several of these studies have focused on the Shan-Thai and Indo-China Terranes, whose collision occurred during the late Jurassic period (Stokes et al. 1996). Geological structures have been shaped by these tectonic events, which have contributed to the formation of diverse regions within the country. Previous geological studies have provided insights into various aspects of the geology of Thailand (Cobbing 2011; Hansen and Wemmer 2011; Ridd et al. 2011; Searle and Morley 2011). According to Bhongsuwan and Ponathong (2002), Thailand is divided into the Shan-Thai Terrane in the west and the Indo-China Terrane in the east.

The main geological structures of the region, characterised by Morley et al. (2011), are outlined in Figure 1. Among these structures, the Southern Thailand region, situated in Peninsular Thailand, features crust in the Upper Peninsular area that dates back to the Cambrian era (Lin et al. 2013). Adjacent to this, the Western Highlands are prominently positioned in the eastern segment of the Shan-Thai Terrane, a geological region that extends from Thailand into neighbouring Myanmar and Malaysia. Comprised of metamorphic rocks, the Shan-Thai Terrane plays a vital role in the geology of the region. Within the Indo-China Terrane, the Khorat Plateau occupies a significant portion of north-eastern Thailand. This expansive region, characterised by a sedimentary thickness that ranges from 3,000 to 4,000 metres (Kozar et al. 1992; Laske et al. 2013), is predominantly composed of Mesozoic and Upper Cretaceous sediments (Lovatt et al. 1996). The Khorat Plateau's geological characteristics make it an indispensable feature for understanding seismic wave propagation within the region. Nevertheless, the deep structures of the region remain elusive, with a conspicuous absence of sufficient geophysical evidence to facilitate a comprehensive understanding.

Granite belts in Thailand, including the Eastern, Central and Western Belts (Charusiri et al. 1993), are mainly located in the Shan-Thai Terrane and distributed throughout the country except for the Khorat Plateau. These belts exhibit a trend from the north to the south. The Eastern Granite Belt consists of Upper Palaeozoic sedimentary and volcaniclastic sequences, as well as granite activities from the Carboniferous to Late Triassic. Between the Eastern Granite Belt and the Khorat Plateau, the boundary coincides with the boundary between the Shan-Thai and Indo-China terranes. The Central Granite Belt covers most of Thailand, excluding the western and north-eastern parts (Charusiri et al. 1993) and primarily consists of Late Palaeozoic to Early Mesozoic clastic sedimentary rocks (Charusiri et al. 1993). The Western Granite Belt trends in the north–south direction and comprises Permian to Carboniferous clastic sedimentary rocks without contemporaneous volcanism (Charusiri et al. 1993).

Recent advances in seismological research in Thailand have provided important information on crustal structures, fault systems, geothermal sources, Moho depth, 1-D velocity models, and anisotropy. For instance, Saetang et al. (2018) utilised body-wave travel-time tomography to examine geothermal sources located beneath the crust of Northern Thailand. The geometries of the Phayao Fault Zones were derived from the focal mechanisms of Mw 6.3 earthquakes

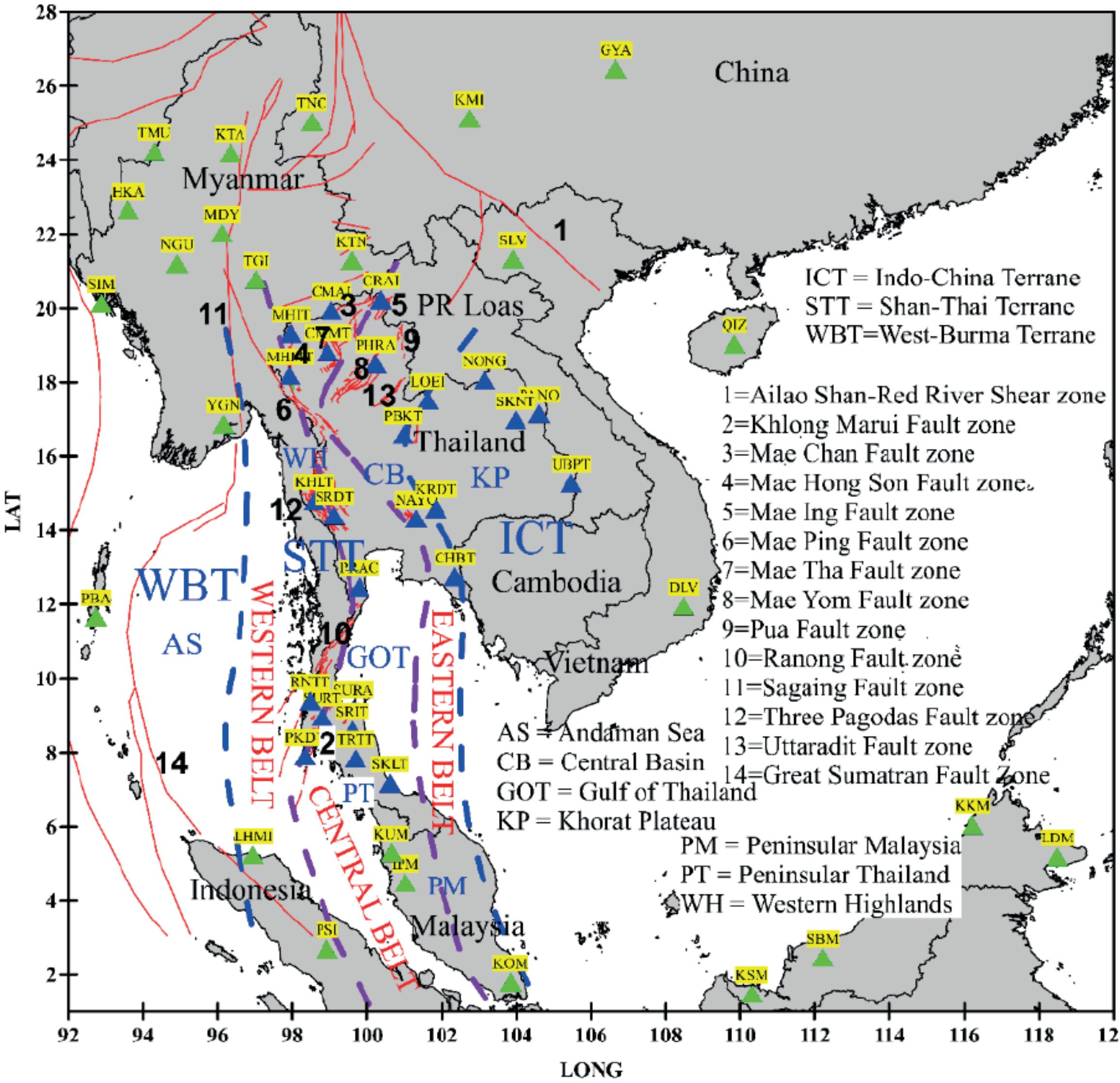

Fig. 1. Highlights basins, granite belts, and highlands in Thailand and nearby regions. Blue and green triangles mark TM and other seismic stations. Blue dashed lines show terrane boundaries; purple dashed lines indicate granite belts; red lines mark faults. Adapted from Charusiri et al. (1993), DMR (2007), and Morley et al. (2011)

and their subsequent aftershocks, as reported by Noisagool et al. (2016), Pananont et al. (2017) and Saetang (2017). Moho lies beneath Thailand, with depths ranging from 28 to 42 kilometres (Noisagool et al. 2014). An analysis of shear-wave splitting suggested that the Shan-Thai and Indo-China Terranes move in a south-eastern direction, while the West-Burma Terrane moves northward (Saetang 2022). Moreover, a minimum 1-D velocity model of northern Thailand was developed, demonstrating a reduction in the root-mean-square of travel time residuals and highlighting correlations between station delays and near-surface geology (Saetang and Durrast 2023).

The geomorphology of Thailand and its surrounding regions is complex and multifaceted, and it holds a pivotal position in the interpretation of seismic research, such as Rayleigh-Wave Group-Velocity Mapping using the ANT. Thailand is situated on the Sunda Plate, part of the larger Indo-Australian Plate, and the interactions between the Sunda Plate and neighbouring plates, such as the Eurasian Plate, create significant seismic activity in the region. The collision between the Indian and Eurasian Plates has formed the Himalayan Mountain range and the Tibetan Plateau, extending into northern Thailand and contributing to seismic activity. Due to the complex geology of Thailand, Rayleigh-Wave Group-Velocity Mapping using The ANT is an essential tool for understanding the subsurface structure. Researchers can create detailed maps of the subsurface by analysing seismic noise, which can reveal geological features that may not be apparent through other methods. Understanding these features will help in interpreting the results of the ANT, providing insights into the subsurface geology and potential seismic hazards. This study utilises geological information and published geoscience research to interpret Rayleigh-wave group-velocity models, such as those between the Shan-Thai and Indo-China Terranes, as well as the boundary of the West-Burma Terrane and Shan-Thai Terrane.

The extensive coverage of broadband stations in Thailand facilitates the estimation of Rayleigh-wave group-velocities through the ANT, a technique that has been extensively employed to image subsurface structures (Shapiro et al. 2005; Yang et al. 2007; Shirzad and Shomali 2014; Wang et al. 2017). This study aims to utilise the ANT to develop comprehensive Rayleigh-wave group-velocity maps for Thailand and its surrounding regions. The derived velocity maps will be examined for correlations with known geological structures, particularly in the Indo-China, West-Burma and Shan-Thai terranes. The accuracy and reliability of the ANT as a tool for capturing subsurface structures will be assessed by comparing the results with existing geological data. The use of the ANT in this study not only demonstrates its potential as a powerful tool for representing subsurface structures in seismically active areas but also paves the way for further studies in other geological settings. Ultimately, this research aims to provide valuable geophysical evidence that enhances the current understanding of deep structures in Thailand and its surrounding regions.

Data and methods

Data collection and preprocessing

In this study, we used the ANT method to extract surface waves through cross-correlation, employing a set of tomographic techniques. Rayleigh waves were specifically used, with the vertical components recorded by a total of 52 seismic stations, including 26 from the Thai Meteorological (TM) Network and 26 from surrounding networks. These recordings were applied to calculate the waveforms. Data were obtained directly from the DMC Web Services and encompass the period from the stations' deployment up to May 2018, as illustrated in Figure 2. The TM network includes seismometers with corner frequencies of 1, 30 and 120 seconds. However, due to the attenuations and scattering experienced along ray paths, dispersion measurements from the short-period stations (1s) were deemed impossible. Consequently, these seismometers were excepted, resulting in a final selection of 26 stations. Based on the data from surrounding networks, only broadband stations were selected, with the number of stations per month shown in Figure 2.

The ANT method was applied following the methodology described by Goutorbe et al. (2015). The data processing stage was meticulously executed, beginning with monthly stacking for each individual station. Several preprocessing steps were followed, including the removal of instrument response, daily trends and mean values. A critical part of this process was the application of band-pass filtering, designed to emphasise signals within the appropriate period range. For shorter period analysis (6–10s), we used a 3–60s band-pass filter, while for longer periods (>10s), we used a 7–60s filter to avoid spectral leakage effects, following

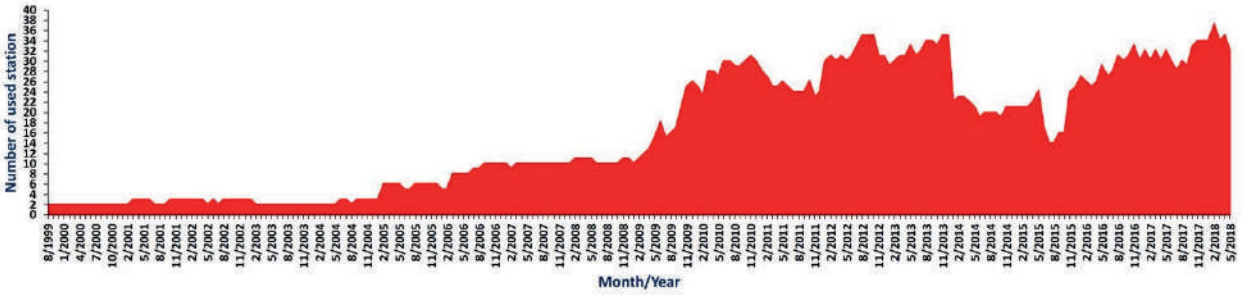

Fig. 2. Duration of Seismic Recordings. The exact time duration of seismic recordings used to obtain the cross-correlations

Goutorbe et al. (2015). This technique facilitated the visualisation of the most energetic surface waves that typically manifest following earthquakes, as described by Bensen et al. (2007) and Lin et al. (2007). To ensure consistency across the data, the signal sampling frequency was standardised at 1 Hz, in accordance with the resampling frequency of 1.0 Hz. Additionally, spectral whitening was applied to flatten the amplitude spectrum within the respective frequency bands, following step (5) of Bensen et al. (2007) and as implemented by Goutorbe et al. (2015).

Cross-correlation and dispersion curve extraction

The continuous waveform data from the seismic stations were processed using the cross-correlation method, following the detailed methodology presented by Bensen et al. (2007). This study utilised seismic waveforms to calculate the cross-correlation between all feasible station pairs, resulting in a comprehensive set of 1,034 pairs across the 52 stations. Subsequently, the dispersion curves for the Rayleigh-wave group velocity were extracted from the cross-correlation. This extraction was performed using frequency-time analysis (FTAN) techniques, as proposed by Levshin and Ritzwoller (2001) and further elaborated by Bensen et al. (2007). The entire process was automated, including both the FTAN and the measurement of dispersion curves from cross-correlation. A critical aspect of the analysis was the consideration of the Signal-to-Noise Ratio (SNR) and the uncertainty associated with velocity measurements.

In our study, the SNR serves as a key quality metric. It helps us assess the dispersion measurements, which we computed within the time domain. Specifically, the signal level was determined from the peak amplitude found in the signal windows, while the noise level was estimated through the root-mean-square (RMS) method applied to the noise windows. To enhance the analysis, the uncertainty of velocity measurements was assessed based on the seasonal variations observed in the dispersion curves. These curves were systematically stacked over three months, allowing for a maximum of 12 stacks to be generated. The stacks were formed from subsets of the input waveforms, grouped into specific monthly combinations, such as Jan–Feb–Mar or Feb–Mar–Apr. The standard deviations (SD) of the group velocity for each period and station pair were subsequently computed from these 3-month stacks, a process that is visually depicted in Figure 3.

From the recorded data, a total of 1,034 pair dispersion curves were obtained. To ensure the integrity and quality of these dispersion measurements before integrating the velocity and period values into the tomographic analysis, specific criteria were meticulously established. One of the primary considerations was the minimisation of natural noise effects and the improvement of input source strength for stringent quality control. This was accomplished by setting a minimum SNR beginning for the station pairs, with the selection of group velocities controlled by the condition that the SNR must be greater than or equal to the defined minimum spectral SNR value of 2 for retaining velocity, and the standard deviation (SD) must be less than or equal to maximum standard deviation of 0.1 km/s. Additionally, the SNR must be greater than or equal to minimum SNR of 15 if no standard deviation is present. The calculation of the SNR involved dividing the peak absolute amplitude in the signal window by the standard deviation found in the noise window, with the signal window defined according to the parameters defining the signal window velocity range of 2.0 to 4.0 km/s. Following Goutorbe et al. (2015), the noise window starts 500 seconds after the signal window and has a width of 500 seconds.

In cases where specific period bands were designated, such as period bands spanning [(4, 7), (7, 15), (10, 22), (15, 30), (20, 35)] seconds, the SNR was computed individually for each band. This was done by first applying a band-pass filter to the cross-correlation using a Butterworth filter, followed by the calculation of the SNR for each centre period and given alpha value of 20. A Gaussian filter was also applied to the cross-correlation, which allowed for the precise calculation of the SNR for each specific period. The signal window was carefully defined to include the range of distance divided by the maximum group velocity (distance/V_{max}) to distance divided by the minimum group velocity (distance/V_{min}), where 'V' symbolises the group velocity. In the FTAN analysis, parameters were defined to control the periods and velocities. The raw and cleaned FTAN periods were both set with a range of 3.0 to 45.1 seconds with 1.0-second steps, while the FTAN

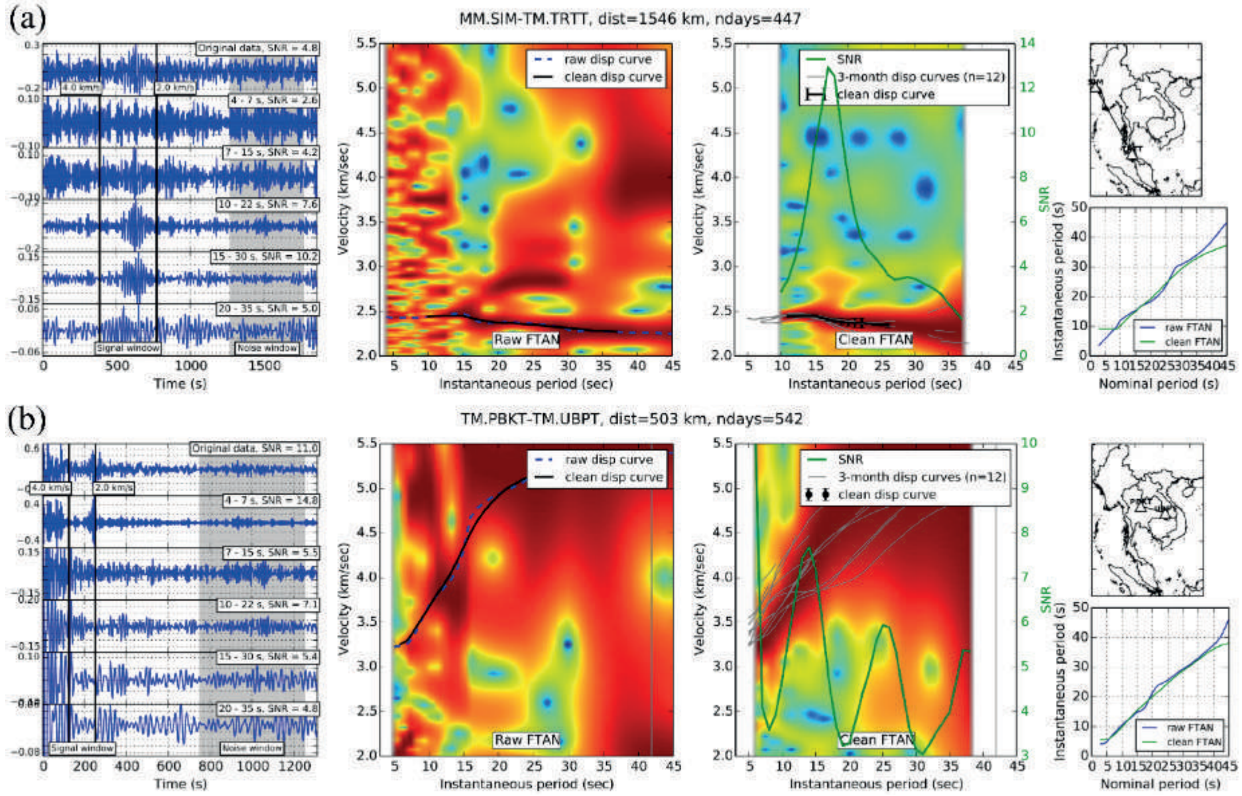

Fig. 3. Dispersion Curves and Frequency-Time Analysis (FTAN). (a) Accepted dispersion curve (SNR ≥ 2, SD ≤ 0.1 km·s^{-1}). (b) Rejected dispersion curve (SNR ≥ 2, SD > 0.1 km·$^{s-1}$). Columns: original and filtered waveforms; raw and clean FTAN of group velocity dispersion curves (filtered 15–50s); map of two station pairs (top fourth column); comparison of raw and clean FTANs (bottom fourth column)

velocities were defined from 2.0 to 5.51 km/s with 0.01-km/s steps. These parameters guided the range and intervals analysed in the FTAN process.

Tomographic inversion

In this study, the tomographic method employed aligns with the approach put forth by Barmin et al. (2001) to reconstruct the Rayleigh-wave group-velocity maps. These maps were created for selected periods on a 0.5°×0.5° geographical grid within the defined study area. A specific penalty function, as expressed in Equation 1 (Barmin et al. 2001), was selected and minimised to derive a model (m) that represents slowness perturbations across the nodes of a uniform grid (Goutorbe et al. 2015).

$$(G(m)-d)^T C^{-1}(G(m)-d) + \propto^2 \|F(m)\|^2 + \beta^2 \|H(m)\|^2$$

In this equation, *d* symbolises the travel time perturbation between station pairs, derived from surface wave data. The essential travel path information, required to integrate this perturbation, is contained within *G* (Barmin et al. 2001; Goutorbe et al. 2015). Meanwhile, *C* serves as the data covariance matrix, accounting for any observational errors in the measured travel times. The function *H*(*m*) imposes a penalty on the model, reflecting the path density in regions characterised by isotropic structures and azimuthal distributions. Equation 2 introduces F(m), a spatial smoothing function applied to the 2-D tomographic map:

$$F(m) = m(r) - \int_S S(r,\acute{r})m(\acute{r})d\acute{r} \tag{2}$$

The smoothing function S(r,r′) is further defined by Equations 3 and 4:

$$S(r,\acute{r}) = K_0 exp\left(-\frac{|r-\acute{r}|^2}{2\sigma^2}\right) \tag{3}$$

$$\int_S S(r,\acute{r})dr = 1 \tag{4}$$

Here, *r* represents the position vector on the grid's surface nodes, and σ is the spatial smoothing width or correlation length. The damping parameters *α* and *β* control the distributions of *H*(*m*) and *F*(*m*) in Equation 1. These parameters, along with σ, can be user-defined through variables, as detailed in Table 1.

The main methodology of the parameter tests was based on the two-pass inversion methodology of Goutorbe et al. (2015), with modifications made to the grid steps and the SNRs. This approach provided a standardised and proven framework for the inversions, while allowing for specific adjustments to suit the unique characteristics of the study area. In the process of conducting parameter tests for this study, a single-pass approach was employed, distinct from the full inversion process that often involves a two-pass method. The parameter tests were designed to systematically explore the variations and impacts of selected parameters, including periods, grid steps, SNRs, correlation lengths and strength parameters. Unlike the full inversion, where a second pass might be used to refine the results and enhance the accuracy, the parameter tests were focused on a broader examination of the parameter space. This one-pass method allowed for a more streamlined and efficient analysis, providing valuable insights into the relationships between different parameters and their effects on the tomographic inversions.

Table 1. Defined Parameters

Parameter	**Value**	**Description**
PERIODMIN_EARTHQUAKE	15.0	Minimum period for earthquake signals
PERIODMAX_EARTHQUAKE	50.0	Maximum period for earthquake signals
PERIOD_RESAMPLE	1.0	Resampling period
MINSPECTSNR	2	Minimum spectral SNR value
MAXSDEV	0.1 km/s	Maximum standard deviation
MINSPECTSNR_NOSDEV	15	Minimum spectral SNR value without standard deviation
SIGNAL_WINDOW_VMIN	2.0	Minimum value for signal window
SIGNAL_WINDOW_VMAX	4.0	Maximum value for signal window
PERIOD_BANDS	[[4, 7], [7, 15], [10, 22], [15, 30], [20, 35]]	Specific period bands
FTAN_ALPHA	20	Alpha value for FTAN
RAWFTAN_PERIODS_STARTSTOPSTEP	[3.0, 45.1, 1.0]	Start, stop, and step values for raw FTAN periods
CLEANFTAN_PERIODS_STARTSTOPSTEP	[3.0, 45.1, 1.0]	Start, stop, and step values for cleaned FTAN periods
FTAN_VELOCITIES_STARTSTOPSTEP	[2.0, 5.51, 0.01]	Start, stop, and step values for FTAN velocities
Discretization grid	0.5° x 0.5°	Geographical grid resolution, representing a spatial sampling of 0.5° latitude by 0.5° longitude
α	Strength of the spatial smoothing term	3000, 200*
σ	Spatial smoothing width	50 km
β	Strength of the norm penalization term	200
λ	Sharpness of the norm weighting function's decrease	0.3

Two minimum spectral SNRs were utilised to filter out low-quality observed velocities: SNR=2 following Saetang (2022), SNR=4 following Shapiro et al. (2005) and SNR=7 following Goutorbe et al. (2015). The SNR is a critical measure of the quality of the seismic data, and the selection of these specific SNRs allowed for a robust assessment of the data quality based on established methodologies. The systematic variation of these parameters, including periods, grid steps, SNRs, correlation lengths, alphas, betas and lambdas, allowed for a comprehensive and robust analysis of the seismic characteristics of the region.

By exploring different periods, grid steps, SNRs, correlation lengths, alphas, betas and lambdas, the study was able to create detailed and accurate Rayleigh-wave group-velocity maps. These maps, in turn, facilitated a nuanced understanding of the subsurface structures and seismic hazards in Thailand and its surrounding regions. The parameter tests underscored the importance of careful parameter selection in seismic tomography, highlighting the complex interplay between data quality, spatial resolution, smoothing and penalisation in the inversion process. The selection of suitable parameters was guided by the need to align the tomographic models with the general geology and tectonic setting of Thailand and surrounding countries, ensuring a coherent and contextually relevant representation of the seismic landscape.

After the parameter tests as presented in Table 2, the tomographic inversions were conducted by adjusting several values to analyse the variations in seismic wave propagation. Two distinct periods – 6 and 10 seconds – were chosen to represent different seismic wave frequencies. The 6-second period was selected as the minimum period due to its proximity to the surface, making it easier to compare the result with surface geology. Periods of 5 seconds were not sufficient for raypaths, and no raypaths were available for 1–4 seconds. The 10-second period was selected to confirm that the result from the 6-second period was consistent. These choices allowed for a comprehensive examination of the subsurface structures.

Three different grid steps were employed in the study: 0.25, 0.5 and 1 degree. These grid steps were used to discretise the geographical area into a grid, with each node representing a specific location. The variation in grid steps allowed for a detailed analysis of the spatial resolution, with smaller grid steps providing higher resolution. Reducing the grid steps from 1 degree to 0.25 degrees increased the time of inversion for each round and necessitated additional Random Access Memory (RAM) for computational processes, but it was deemed necessary. The grid steps should be lower than the average distance between stations, ensuring a more accurate representation of the seismic landscape.

Correlation lengths of 50, 150 and 250 km were used to control the spatial smoothing in the penalty function. The correlation length is a measure of how the slowness perturbations are correlated across different spatial nodes. By varying the correlation length, the study explored the impact of spatial smoothing on the tomographic results.

Table 2. Parameter Tests for Tomographic Inversions

Parameter	Description	Values Used
Periods	Distinct periods for seismic wave frequencies	6s, 10s
Grid Steps	Discretize the geographical area into a grid	0.25, 0.5, 1 degree
Minimum Spectral SNRs	Filter out low-quality observed velocities	2, 4, 7
Correlation Lengths	Control spatial smoothing in the penalty function	50, 150, 250 km
Strength Parameter Alpha	Control spatial smoothing term in the penalty function	200, 400, 600
Beta Value	Control strength of the norm penalization term	200
Lambda Value	Control sharpness of the norm weighting function's decrease	0.3

Three different values of the strength parameter alpha (200, 400, 600) were employed to control the spatial smoothing term in the penalty function. The variation in alpha allowed for a systematic investigation of the trade-off between data fit and model smoothness. A constant beta value of 200 was used to control the strength of the norm penalisation term, and a lambda value of 0.3 was employed to control the sharpness of the norm weighting function's decrease. These parameters were carefully selected to penalise the weighted norm of the parameters, ensuring a robust and reliable tomographic inversion.

Two-pass inversion and final inversion

The inversion process in this study was conducted in two distinct passes, following the methodology described by Barmin et al. (2001). Each pass involved a specific set of parameters, following the algorithm described by Barmin et al. (2001).

First Pass: The initial pass involved an overdamped tomographic inversion. During this phase, the travel-time residuals between observed and predicted travel-times for all pairs of stations were carefully evaluated. The primary objective of this pass was to create smooth velocity maps, emphasising a substantial spatial smoothing effect, with a damping parameter α = 3000, as detailed in Table 1.

Second Pass: Following the first pass, which is used to identify and reject outliers, any pairs with absolute residuals exceeding three times the standard deviation of the residuals were excluded. This two-pass approach aims to improve the reliability of the tomographic inversion by removing pairs that might introduce errors or noise into the inversion process. The second tomographic inversion was then carried out, employing parameters specifically chosen to ensure that the resulting Rayleigh-wave group-velocity maps would accurately depict regional geological structures and correspond with recognised geological information. In this phase, the values of σ, α and β were set at 50, 200 and 200, respectively (as referenced in Table 1).

The final inversion, conducted after the two-pass process, utilised optimal parameters identified through the parameter tests (Table 2). This stage synthesised insights from previous inversions to create accurate Rayleigh-wave group-velocity maps. By considering data quality, spatial resolution, smoothing and penalisation, the final inversion ensured that the tomographic models aligned with the geology and tectonic setting of Thailand and surrounding areas, providing a coherent representation of the seismic landscape.

Spatial resolution assessment

The assessment of the spatial resolution in the tomographic inversion was conducted in alignment with the methodologies established by Lévěque et al. (1993) and Barmin et al. (2001). The resolution matrix (R) is formulated as per Equation 5:

$$R = (G^T C^{-1} G + Q)^{-1} G^T C^{-1} G \qquad (5)$$

This equation is derived from the forward problem, as expressed in Equation 6:

$$\widehat{m} = G^t C^{-1} \delta t = (G^t C^{-1} G) m = Rm \qquad (6)$$

Here, Q represents a matrix that encapsulates the influence of a Gaussian spatial smoothing operator, and G^t is the inverse operator, defined by Equation 7:

$$G^t = (G^T C^{-1} G + Q)^{-1} G^T \qquad (7)$$

The resolution maps, as presented in the Results and Discussion section, were constructed using this mathematical framework. Each row of the resolution matrix corresponds to an individual resolution map, assessing the resolution at a specific spatial node. The i-th row of the resolution matrix contains the resolution map linked to the i-th grid node (Goutorbe et al. 2015). By fitting a cone centred on each node to the corresponding resolution map, the radius of the cone serves as an indicative measure of the spatial resolution at that particular node.

Results and discussion

Parameter tests and their effects

In our analysis of the seismic data, we tested several parameters to gauge their impact on the observed

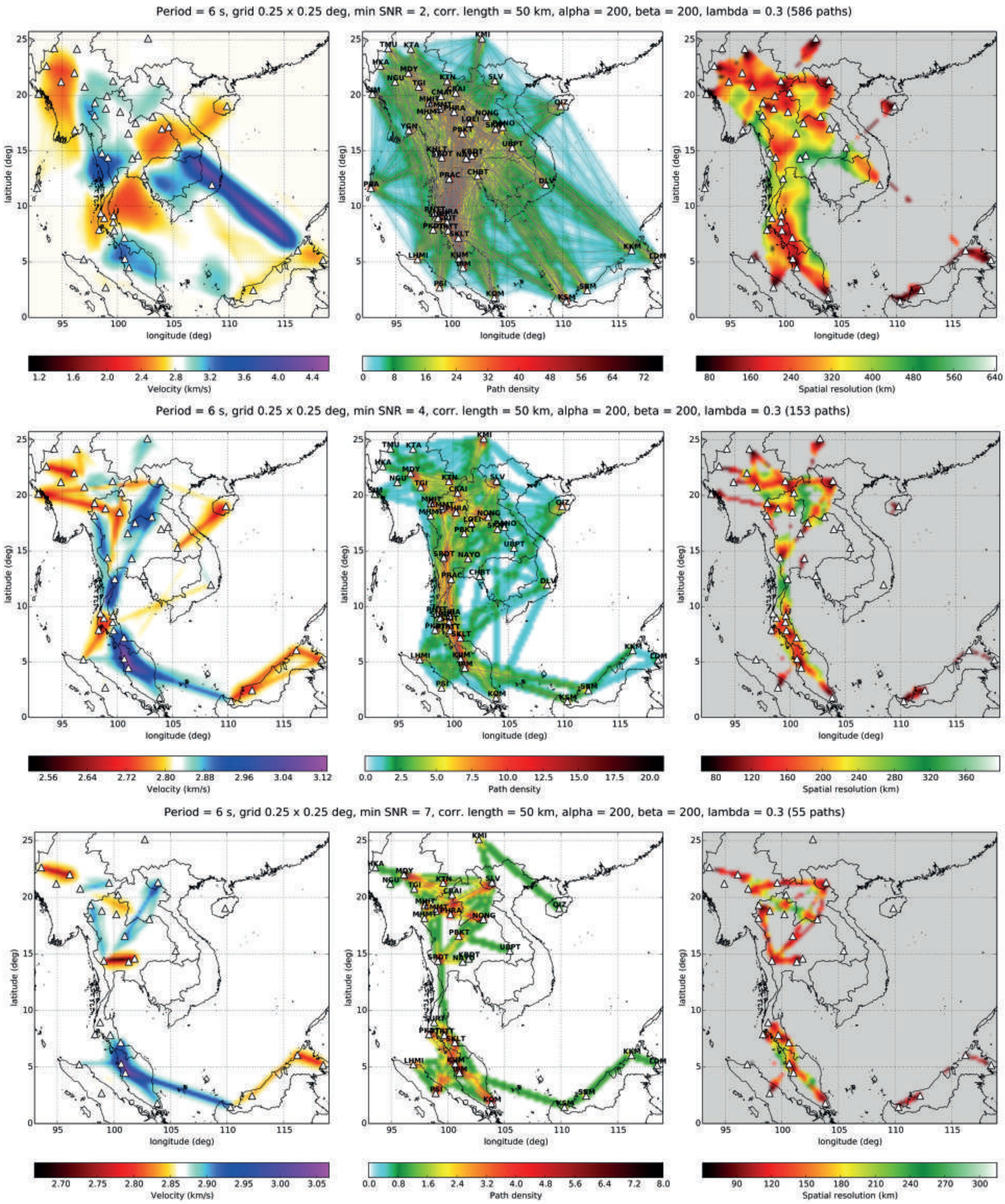

Fig. 4. SNR Analysis. The figure illustrates the impact of varying SNRs (2, 4, 7+) on tomographic inversions, focusing on Rayleigh wave velocity, path density, and spatial resolution. As SNR increases, the number of input dispersion curves decreases: 586 for SNR=2, 153 for SNR=4, and 55 for SNR=7. The analysis is conducted with a fixed grid spacing of 0.25 degrees and set parameters for spatial smoothing (200), smoothing width (50 km), norm penalisation (200), and norm function sharpness (0.3)

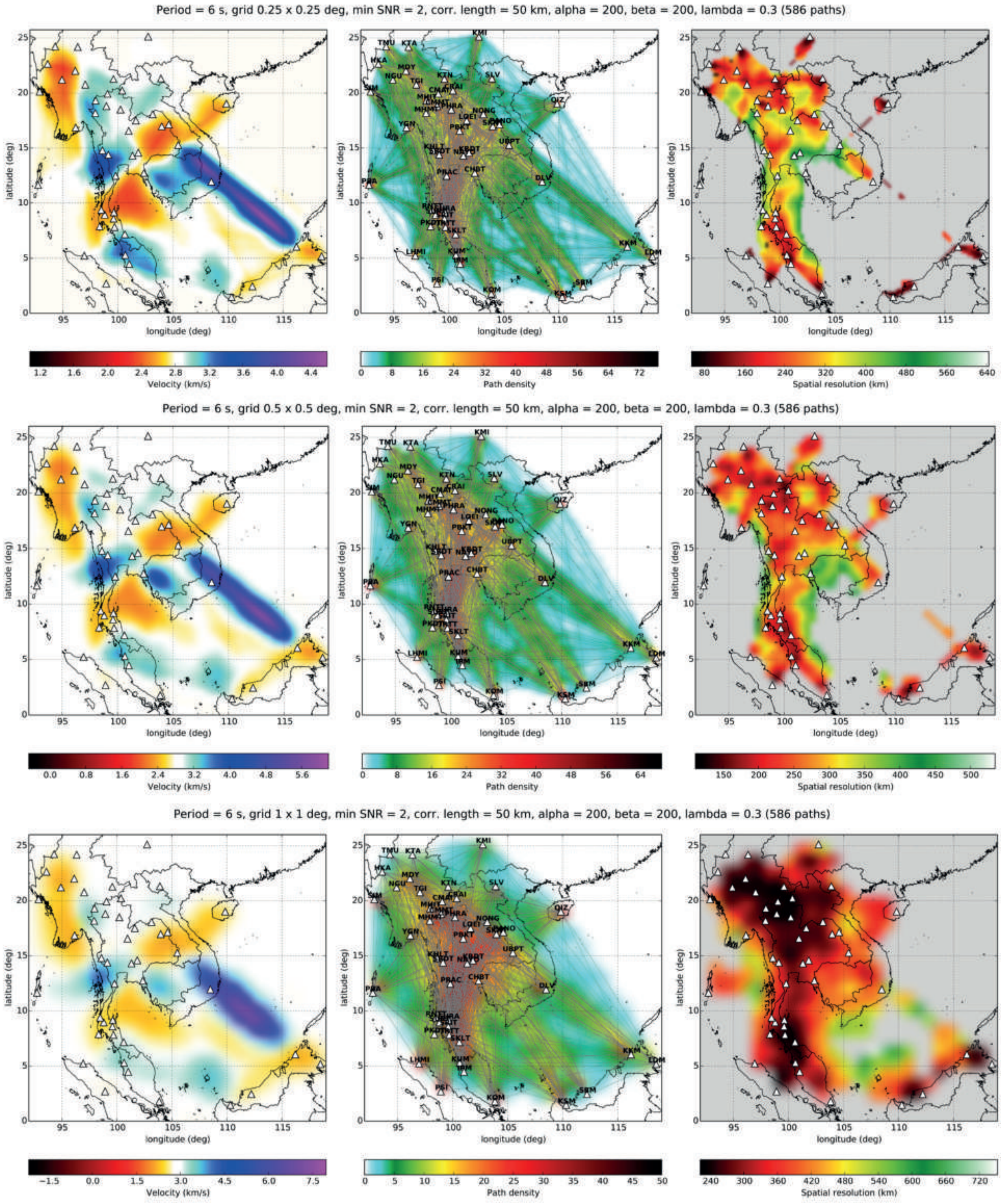

Period = 6 s, grid 0.25 x 0.25 deg, min SNR = 2, corr. length = 50 km, alpha = 200, beta = 200, lambda = 0.3 (586 paths)

Period = 6 s, grid 0.5 x 0.5 deg, min SNR = 2, corr. length = 50 km, alpha = 200, beta = 200, lambda = 0.3 (586 paths)

Period = 6 s, grid 1 x 1 deg, min SNR = 2, corr. length = 50 km, alpha = 200, beta = 200, lambda = 0.3 (586 paths)

Fig. 5. Grid Spacing Impact on Tomographic Inversions. This figure compares the effects of grid spacings (0.25, 0.5, 1) on Rayleigh wave velocity, path density, and spatial resolution. Fixed parameters include spatial smoothing (200), smoothing width (50 km), norm penalization (200), and a minimum SNR of 2. The left column shows velocity variations, the centre column maintains consistent ray-path coverage, and the right column reveals spatial resolution differences. Grid spacing of 0.25 maximises resolution but lacks coverage; 1 degree maximises coverage but lowers resolution; 0.5 degree offers a balanced trade-off.

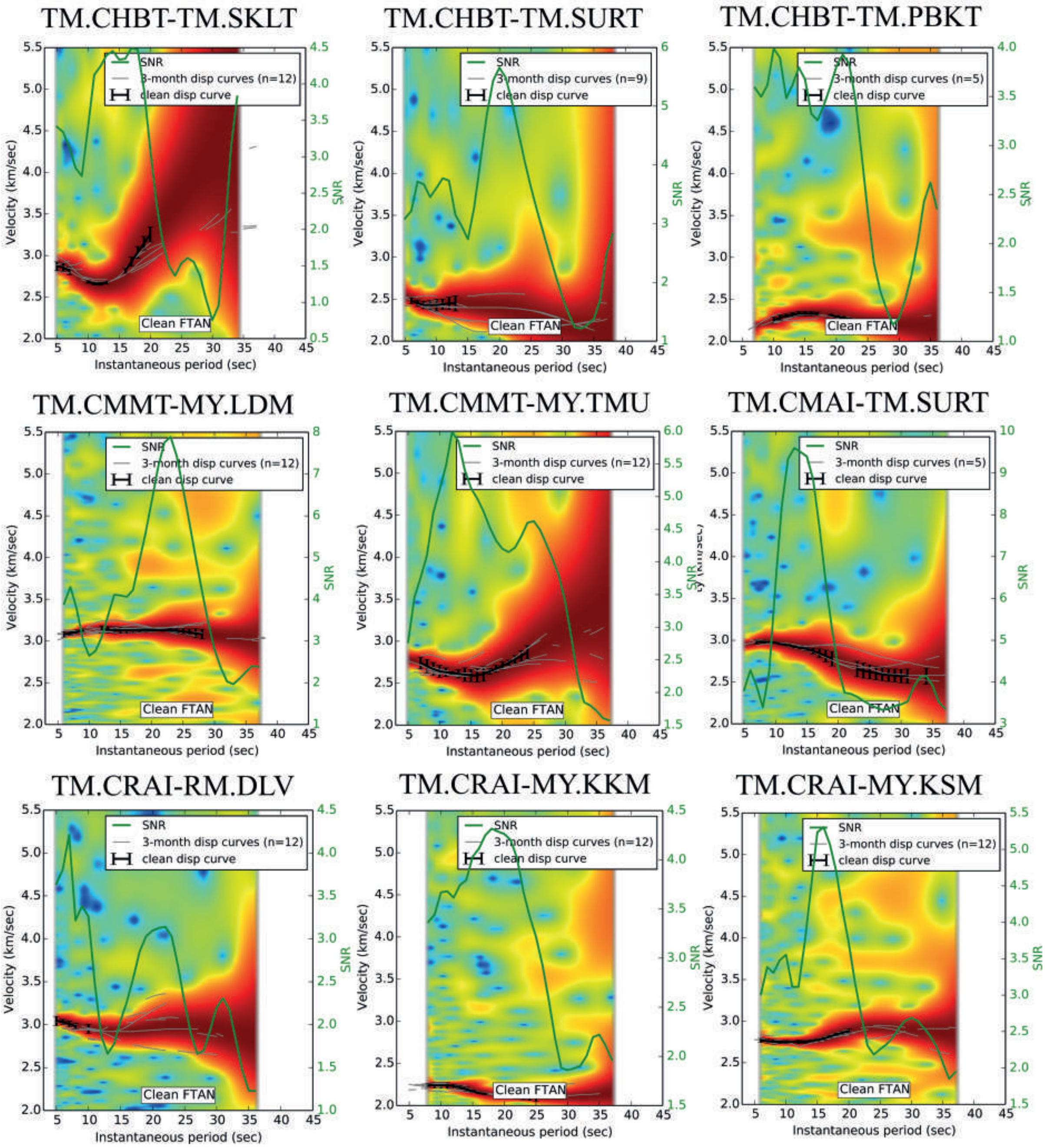

Fig. 6. Dispersion Curve Analysis for SNR >= 2 and SD <= 0.1 km/s. This figure illustrates dispersion curves where SNR is aimed to be close to 2 but also maintained at or above this threshold, optimising clarity and reliability for tomographic inversion

seismic phenomena. The specific parameters and their variations are detailed in Table 2. Among these, the most critical and influential parameters were identified and are illustrated in Figs. 4 and 5. Figures 4 and 5 illustrate the comparison of certain parameters. However, the authors considered the results from all parameters listed in Table 2 to select the most suitable ones for full tomographic inversions. The final selection of parameters is presented in Table 1. This selection was made by considering the surface geology and tectonic settings at the study area and also considering the spatial resolution and ray-path coverage.

In Figure 4, we analyse SNR and its impact on tomographic inversions. The grid spacing is fixed at 0.25 degrees, and parameters for spatial smoothing and penalisation are also set. The figure includes variations in SNR values: 2 for the top row, 4 for the middle row and 7 or greater for the bottom row. As the SNR increases, we observe a decrease in the number of input dispersion curves: 586 for SNR=2, 153 for SNR=4 and 55 for SNR=7. Despite this, an SNR of 2 or greater shows more input dispersion than an SNR of 4 or 7. While higher SNR values indicate better quality, an SNR of 2 or greater remains acceptable if the standard deviation (SD) is less than or equal to 0.1 km/s. This criterion ensures that dispersion curves with SNR greater than or equal to 2 are suitable for tomographic inversion, as further demonstrated in Figure 6.

Figure 5 examines the influence of grid steps on Rayleigh-wave group-velocity (left column), path density in km (centre column), and spatial resolution (right column) within tomographic inversions. The analysis was conducted with variations in grid spacing values of 0.25 (Top Row), 0.5 (Middle Row) and 1 (Bottom Row) and includes fixed parameters such as the Strength of the spatial smoothing term (200), Spatial smoothing width (50 km), Strength

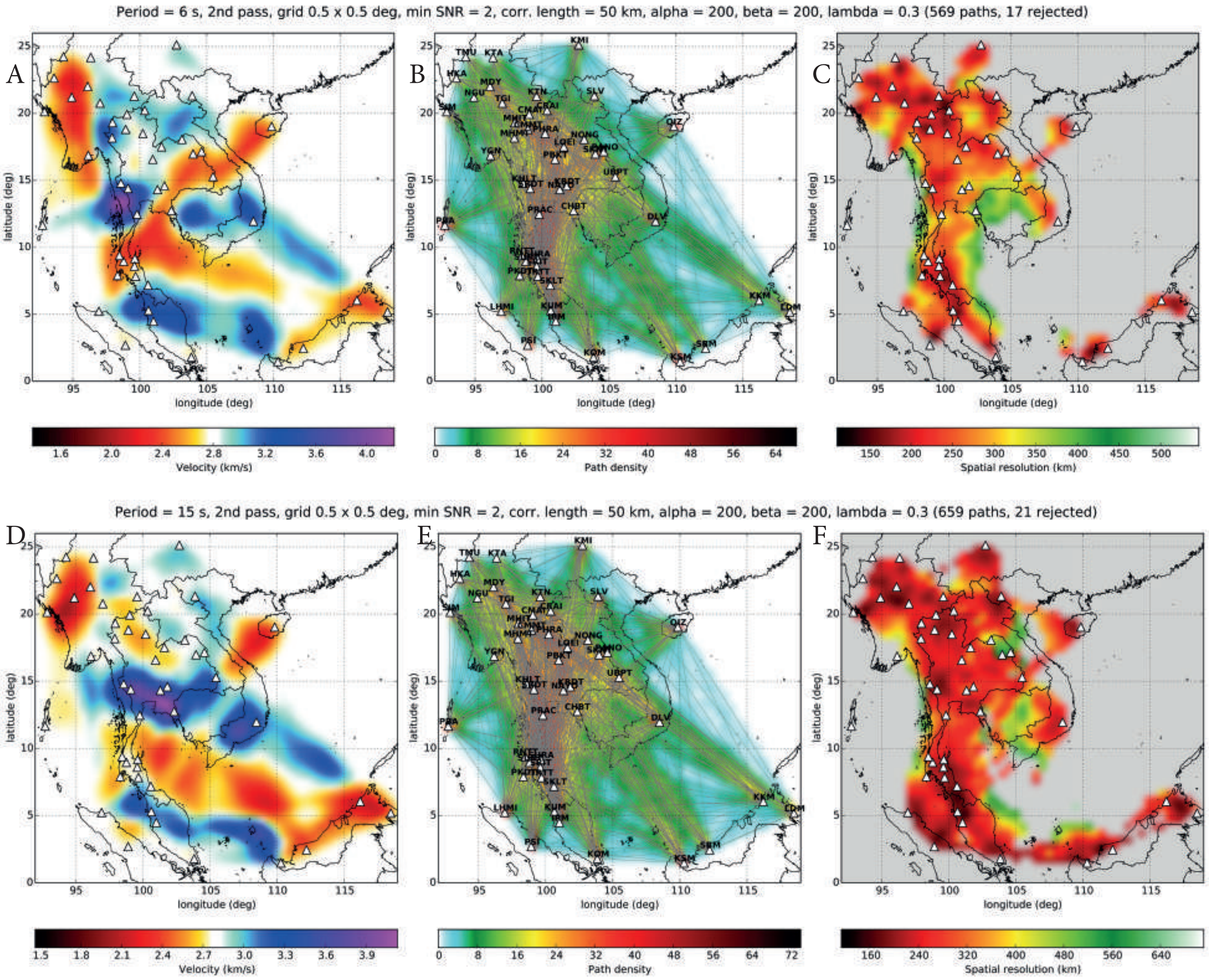

Fig. 7. Rayleigh-wave group-velocity maps of Thailand and adjacent areas at 6-second and 15-second periods. (A) Group velocity at 6 seconds. (B) Path density at 6 seconds. (C) Spatial resolution at 6 seconds. (D) Group velocity at 15 seconds. (E) Path density at 15 seconds. (F) Spatial resolution at 15 seconds. Gray zones indicate areas with undefined resolution; white triangles mark seismic stations. The 6-second period is sensitive to upper crustal structures, whereas the 15-second period is sensitive to deeper structures potentially associated with the mid-crustal Conrad discontinuity

of the norm penalisation term (200), and Sharpness of the norm weighting function's decrease (0.3), alongside a fixed SNR of 2 or greater. The left column of Figure 5 illustrates lateral variations for lower and higher velocity groups, represented by red and blue colours, respectively. Although the automatic colour scale is uniform, the middle column, which represents ray-path coverage, does not exhibit significant differences. In contrast, the right column reveals noticeable disparities in spatial resolution. The top box in the left column, with 0.25 grid spacing, offers the highest resolution (over 80 km, red) but lacks complete coverage. The middle box extends the spatial resolution area but lowers the resolution to over 150 km (red), and the bottom box provides the most coverage with the poorest resolution (over 240 km, red). The selected 0.5 grid spacing balances the resolution with spatial coverage.

In addition to the analysis conducted for the 6-second and 10-second periods, similar parameter tests were performed, and the results were found to be consistent across different seismic wave frequencies. This consistency further validates the selected parameters for tomographic inversions, as shown in Table 1. Table 3, presenting the second pass of tomographic inversion, illustrates this point by detailing the number of raypaths input, accepted and rejected for various periods, using parameters σ=50, α=200 and β=200. Across the periods ranging from 6 to 20, the acceptance rate remained consistently high, ranging from 96.8% to 97.5%, while the rejection rate varied slightly between 2.5% and 3.2%. This pattern signifies a well-constrained inversion, leading to more accurate tomographic images.

Final inversion

The ANT of Rayleigh waves conducted across Thailand and its surrounding regions has yielded invaluable insights into the subsurface structure and crustal properties. Utilising seismic network data, we constructed group-velocity maps for multiple periods, revealing significant lateral variations in seismic velocities. This work builds upon previous studies (Lin et al. 2007; Yang et al. 2007; Shirzad and Shomali 2014).

The inversion process was executed in two stages, as outlined in Table 2. The first stage aimed to create smooth velocity maps, while the second stage refined these by removing outliers and noise. Optimal parameters were identified through rigorous testing (Table 1), and the final inversion synthesised these insights to produce accurate Rayleigh-wave group-velocity maps. By considering factors like data quality, spatial resolution, smoothing and penalisation, we ensured alignment with the geology and tectonic settings of Thailand and its surrounding areas.

Significantly, our research categorises Rayleigh-wave group-velocity maps into two critical frequency bands, one ranging from 6 to 13 seconds and another from 14 to 20 seconds. These bands consistently display characteristics of both lower and higher velocities. Within these frequency ranges, the 6-second and 15-second periods emerge as essential benchmarks for our study. Specifically, the 6-second period is highly sensitive to near-surface geological features, while the 15-second period provides crucial insights into deeper geological structures, potentially associated with the mid-crustal Conrad discontinuity. Variations in surface geology can have a notable impact on the velocities observed at these key periods. These are visually represented through an automatic colour scale, with red for lower velocities and blue for higher velocities, implemented using Python code. To facilitate a nuanced interpretation of these findings, Figure 7 presents detailed views of these pivotal periods with six panels (A-F). This figure showcases the group-velocity maps along with complementary maps of path density and spatial resolution. This integrated presentation is designed to focus attention on areas with well-defined, high-resolution data while deliberately omitting areas where resolution is undefined.

The sensitivity of Rayleigh waves to underground structures is period-dependent. Shorter periods (6–13 sec) are generally sensitive to shallower structures, often corresponding to the upper crust (Shapiro et al. 2005; Belovezhets et al. 2021; Kil et al. 2021; Abdelfattah et al. 2023). Conversely, longer periods (14–20 sec), especially the 15-second period, are more sensitive to deeper structures, potentially related to compositional variations, temperature or pressure conditions that differ from the upper crust (Shapiro et al. 2005; Cooper et al. 2017; Poveda et al. 2018). Waves with shorter periods are susceptible to attenuation and scattering from teleseismic earthquakes.

As a general rule, the sensitivity of Rayleigh-wave peaks at depths approximately equal to onethird of their wavelength. Notably, the methodology employed lacks an option for directly translating period ranges into depth sensitivities. To address this, we employed a heuristic approach based on an assumed average group velocity for Rayleigh waves of around 3 km/s. Our analysis suggests that the 6–13-s period range is particularly useful for investigating structures in the upper crust, within an approximate depth range of 6–13 km. The 14–20-s period range, and notably the 15-second period, is presumed to be more relevant for structures at the mid-crustal Conrad discontinuity, starting at approximately 14 km. This is corroborated by noticeable changes in lateral variations of group-velocity structures starting at 14 seconds, with a significant shift observed at 15 seconds. Due to constraints on the allowable number of input dispersion curves, our tomographic inversion methodology is limited in its capacity to generate reliable group-velocity maps for periods extending beyond 20 seconds. Complementing our findings, Siangpipop (2022) reported that the Conrad discontinuity beneath Northern Thailand is shallowest at about 10.9 km in the western province and deepest at around 20.9 km beneath the Phitsanulok Basin.

The 6-sec period

The variations in seismic velocities across different regions can be attributed to a variety of geological factors. For the 6-second period, known for its acute sensitivity to structures in the upper crust and its strong correlation with near-surface geological features, the map identifies regions with group velocities either falling below or exceeding 2.8 km/s.

The observed discrepancy in Rayleigh-wave velocities between the West-Burma Terrane and the Shan-Thai Terrane, particularly at the 6-second period, is a result of a complex interplay of geological, geophysical and methodological factors. Specifically, velocities lower than 2.8 km/s in the West-Burma Terrane and higher than 2.8 km/s in the Shan-Thai Terrane at the Sagaing Fault zone may be attributed to lithological variations. The Shan-Thai Terrane likely comprises rock formations that are more rigid and more dense, such as metamorphic or igneous rocks, leading to higher velocities. In contrast, the West-Burma Terrane may encompass softer geological materials like sedimentary rocks, fractured zones or even geothermal pathways, resulting in lower velocities. These velocity variations are concentrated in two significant regions, each with differing levels of reliability in the velocity model. When cross-referenced with a spatial resolution map, the velocity contrast between the onshore areas of the West-Burma Terrane and the Shan-Thai Terrane is supported by high spatial resolution, providing a high degree of certainty in the velocity model for that area. Conversely, the velocity contrast for the offshore areas between the two terranes is not as well-supported by spatial resolution, leading to reduced reliability in the velocity model for those regions.

The second region involves the Khorat Plateau, extending into southern Thailand and encompassing the Andaman Sea and the Gulf of Thailand. The lower velocities in the Khorat Plateau could be due to the presence of softer, less-consolidated materials like sediments or sedimentary rocks, which usually result in slower seismic wave propagation. A distinct boundary separates the West-Burma Terrane from the Shan-Thai Terrane, characterised by contrasting velocities either below or above 2.8 km/s. The Shan-Thai Terrane contains high-velocity groups but lacks sufficient differentiation to separate its Central, Western and Eastern Belts, suggesting a more heterogeneous composition of the crust in this region.

The Western Highlands, a component of the Western granite belt, hosts the highest velocity group, nearing 4.0 km/s. This elevated seismic velocity can be attributed to a multifaceted set of factors. One primary reason could be the presence of very dense, old and consolidated rocks, possibly granitic in nature. Additionally, the rocks in the area may exhibit low porosity, which generally contributes to higher seismic velocities. The absence of fluid-filled fractures could also be a significant factor in these higher velocities. Thermal conditions of the crust may further influence seismic velocities, as a cooler crust would generally result in higher velocities. Lastly, the area might have undergone significant metamorphism, increasing the density and seismic velocity of the rocks.

In southern Thailand, the upper and lower parts of the low-velocity groups are distinctly separated from the higher velocity groups at the contractual boundaries of the Ranong Fault Zone and the Khlong Marui Fault Zone. At the Ranong Fault Zone, the upper part of the low-velocity groups is separated from the high-velocity groups of the

Western Highlands. Specifically, the left side of this boundary is characterised by the high-velocity group of the Western Highlands, while the dividing line between this high-velocity group and the low-velocity groups on the right side extends to the Khlong Marui Fault Zone.

These boundaries, following a north-east–south-west orientation, serve as natural separators between different geological terranes or units, leading to velocity contrasts in seismic studies. The boundary at the Khlong Marui Fault Zone further delineates low-velocity groups on its left side and high-velocity groups on its right side, with the latter extending into Peninsula Malaysia. This observation is particularly applicable when the terranes have varying rock types or degrees of rock alteration. Additionally, the characteristics of fault zones like the Ranong and Khlong Marui, which consist of crushed, fractured rock, play a pivotal role. These fault zones can act as barriers or conduits for seismic waves, contributing to the observed lower velocities due to their fractured nature. Their orientation could also naturally dictate the orientation of these velocity boundaries. Furthermore, the presence of fluids in these fault zones could also influence seismic velocities; fluid-filled fractures or porous rocks within the fault zones could slow down seismic waves, creating additional velocity boundaries.

The 15-sec period

For the 15-second Rayleigh wave, this period is notably more sensitive to deeper geological structures, potentially associated with the mid-crustal Conrad discontinuity, compared to the 6-second period. Our analysis, supported by 659 accepted raypaths for the 15-second period as opposed to 569 for the 6-second period as detailed in Table 3, uncovers both congruent and divergent patterns of horizontal variations in group velocities. These patterns either corroborate or contrast with findings previously discussed for the 6-second period. The increased number of accepted raypaths for the 15-second period also results in more extensive spatial resolution coverage, as evidenced by a comparison between the right panels of Fig. 7 (continued) and Figure 7. The increased number of accepted raypaths for the 15-second period also results in more extensive spatial resolution coverage, as evidenced by comparing panel F with panel C in Figure 7. The 15-second period reveals a low-velocity group in the West-Burma Terrane, consistent with observations at the 6-second period. The northward movement of the West-Burma Terrane, corroborated by GPS velocity fields (Kreemer et al. 2014), is in accordance with findings from Saetang (2022) that indicate a northward trending flow direction of the lithosphere. Given these data, distinct variations are observed at the boundary between low and

Table 3. Second Pass of Tomographic Inversion: Number of raypaths input, accepted, and rejected for each period, using parameters $\sigma=50$, $\alpha=200$, $\beta=200$

Period	Input	Accepted Number (%)	Rejected (%)
6	586	569 (97.1%)	17 (2.9%)
7	700	680 (97.1%)	20 (2.9%)
8	742	720 (97.0%)	22 (3.0%)
9	754	731 (96.9%)	23 (3.1%)
10	750	731 (97.5%)	19 (2.5%)
11	728	709 (97.4%)	19 (2.6%)
12	715	696 (97.3%)	19 (2.7%)
13	699	679 (97.1%)	20 (2.9%)
14	696	675 (97.0%)	21 (3.0%)
15	680	659 (97.1%)	21 (3.1%)
16	648	628 (96.9%)	20 (3.1%)
17	632	613 (97.0%)	19 (3.0%)
18	603	584 (96.8%)	19 (3.2%)
19	570	554 (97.2%)	16 (2.8%)
20	534	519 (97.2%)	15 (2.8%)

high-velocity groups. In the northern part of the West-Burma Terrane, the boundary orientation is north–south, which is in agreement with the 6-second period and supports the northward flow direction of the lithosphere, as indicated by Saetang (2022). Conversely, the boundary in the southern part of the West-Burma Terrane deviates to a north-east–south-west orientation at the 15-second period. Saetang (2022) does not provide interpretations pertinent to the flow direction of the lithosphere in this southern region.

For the Western Highlands area, the 15-second period also reveals a high-velocity group close to 4.0 km·s^{-1} corroborating the results observed at the 6-second period. However, a notable difference emerges when examining the extent of these high-velocity groups. In the 15-second period, these high-velocity groups extend into the Central Basin and the Khorat Plateau, a contrast to the 6-second period where they are confined to the Western Highlands. Additionally, the high-velocity groups beneath the Western Highlands and the Central Basin align in a south-east–north-west direction, consistent with the orientation of the Mae Ping and Three Pagodas Fault Zones as depicted in Figure 1. These areas are also well-represented in terms of spatial resolution, as evidenced by panel F of Figure 7. The high-velocity groups beneath the Khorat Plateau are well-supported by spatial resolution and lie in a north-east–south-west direction, differing from the direction of high-velocity groups beneath the Central Basin. The change of direction of high-velocity groups beneath the Central Basin and the Khorat Plateau is significantly found at the boundary between the Shan-Thai Terrane and the Indo-China Terrane.

In the southern part of the study area, we observed a low-velocity group beneath the Peninsula of Thailand. This group aligns in a south-east–north-west direction, similar to the high-velocity groups observed beneath the Western Highlands, the Central Basin and the Malaysia Peninsula. It is noteworthy that the upper part of this low-velocity group is connected with the high-velocity group beneath the Western Highlands and the Central Basin. This boundary significantly cuts across the narrowest part of Thailand, extending from the Gulf of Thailand to the Cambodian border at Klong Yai, located in Thailand's south-eastern province of Trat. Additionally, the lower part of the low-velocity group beneath the Peninsula of Thailand is connected with the high-velocity group beneath the Malaysia Peninsula. This latter boundary closely aligns with the international border between Thailand and Malaysia.

Furthermore, a significant difference was observed in Northern Thailand for the 15-second period. Both the West-Burma Terrane and Northern Thailand are marked by the same low group velocity. This contrasts with the 6-second period, where Northern Thailand and the West-Burma Terrane show different colours – blue and white for Northern Thailand and red for the West-Burma Terrane – indicating different velocity groups. This observation could be indicative of varying geological conditions at different depths. In this context, it is of particular significance that Saetang et al. (2018) identified low-velocity anomalies in Northern Thailand through local earthquake tomography, which could be related to this observed low group velocity. Furthermore, the study by Saetang et al. (2018) indicates high Vp/Vs ratios below mountain ranges, potentially aligning with the south-east–north-west directional flow of the lithosphere and asthenosphere as interpreted by Saetang (2022). The contributions of Saetang et al. (2018) regarding the Moho depth and the presence of geothermal sources add another layer of geological complexity, supporting the idea that the low-velocity group in Northern Thailand may not necessarily be connected to the West-Burma Terrane. This uncertainty is partly due to the small area of red colour at the station TGI and is further supported by shear wave splitting data from Saetang (2022), which indicates different flow directions for the lithosphere and asthenosphere beneath the West-Burma Terrane and Northern Thailand. Notably, the low-velocity group in Northern Thailand approximately lies in a south-east–north-west direction, aligning with the flow direction of the lithosphere and asthenosphere as interpreted by Saetang (2022). The eastern part of the low-velocity group at Northern Thailand is approximately terminated at the boundary between the Shan-Thai Terrane and the Indo-China Terrane.

Conclusions

Utilising the ANT and rigorous parameter tests, we explored the seismic characteristics of subsurface structures in Thailand, the Malaysia Peninsula, the

Thailand Peninsula and the Central Basin. Our analyses of Rayleigh-wave group-velocity maps for periods between 6 and 20 seconds revealed significant lateral variations in seismic velocities. High-velocity zones were predominantly associated with the Shan-Thai Terrane, while low-velocity zones were identified in Northern Thailand, the West-Burma Terrane and the Khorat Plateau. In a broader scientific context, our findings both align with and extend previous studies, particularly enhancing our understanding of the seismic landscape from the upper crust to the mid-crustal Conrad discontinuity. The implications of this research are far-reaching, potentially affecting earthquake preparedness and resource exploration in these tectonically active regions. While the study is robust, limitations exist in terms of data quality and the extent of parameter tests conducted. Nevertheless, the rigorous methodology employed and the diverse data sources utilised affirm the effectiveness of ANT as a valuable tool for seismic research in areas with complex geological histories and active tectonic settings.

Acknowledgments

The authors thank TMD and IRIS for seismic data, the network operators and technicians for maintaining the seismic stations in Thailand, and Bruno Goutorbe from the Institut de Physique du Globe de Paris for the computational implementation of the ambient noise tomography. We also thank the Department of Mineral Resources (Thailand) for providing access to their geological database. Appreciation is also extended to the National e-Science Infrastructure Consortium for computing resources. Special acknowledgment goes to IRIS for the instrument metadata created by Portable Data Collection Center software.

Disclosure statement

No potential conflict of interest was reported by the authors.

Author contributions

Study design: KS; data collection: KS, WS; statistical analysis: KS, WS; result interpretation: KS, WS; manuscript preparation: KS, WS; literature revieIn: KS, WS.

References

ABDELFATTAH AK, AL-AMRI A, ALZAHRANI H and ABUAMARAH BA, 2023, Ambient noise tomography in the upper crust of North Harrat Rahat, Saudi Arabia. *Journal of King Saud University – Science* 35(2): 102523. DOI: https://doi.org/10.1016/j.jksus.2022.102523.

BARMIN MP, RITZWOLLER MH and LEVSHIN AL, 2001, A fast and reliable method for surface wave tomography. *Pure and Applied Geophysics* 158(8): 1351–1375. DOI: https://doi.org/10.1007/PL00001225.

BELOVEZHETS NN, BEREZHNEV YM, KOULAKOV IY, SHAPIRO NM, ABKADYROV IF, RYCHAGOV SN and GORDEEV EI, 2021, The structure of the upper crust beneath the Kambalny volcano (South Kamchatka) revealed from ambient noise tomography. *Doklady Earth Sciences* 501(1): 933–937. DOI: https://doi.org/10.1134/S1028334X21110040.

BENSEN GD, RITZWOLLER MH, BARMIN MP, LEVSHIN AL, LIN F, MOSCHETTI MP and YANG Y, 2007, Processing seismic ambient noise data to obtain reliable broad-band surface wave dispersion measurements. *Geophysical Journal International* 169(3): 1239–1260. DOI: https://doi.org/10.1111/j.1365-246X.2007.03374.x.

BHONGSUWAN T and PONATHONG P, 2002, Magnetic Characterization of the Thung-Yai Redbed of Nakhon Si Thammarat Province, Southern Thailand, and Magnetic Relationship with the Khorat Redbed. *ScienceAsia* 28: 277–290.

CHARUSIRI P, CLARK AH, FARRAR E, ARCHIBALD D and CHARUSIRI B, 1993, Granite belts in Thailand: evidence from the 40Ar/39Ar geochronological and geological syntheses. *Journal of Southeast Asian Earth Sciences* 8(1): 127–136. DOI: https://doi.org/10.1016/0743-9547(93)90014-G.

COBBING EJ, 2011, Granitic rocks. In: Ridd MF, Barber AJ and Crow MJ (eds.), *The Geology of Thailand*. Geological Society of London.

COOPER CM, MILLER MS and MORESI L, 2017, The structural evolution of the deep continental lithosphere.

Tectonophysics 695: 100–121. DOI: https://doi.org/10.1016/j.tecto.2016.12.004.

DEPARTMENT OF MINERAL RESOURCES (DMR), 2007, *Geological Map of Thailand*. Ministry of Natural Resources and Environment, Thailand.

GOUTORBE B, COELHO DLD and DROUET S, 2015, Rayleigh wave group velocities at periods of 6-23 s across Brazil from ambient noise tomography. *Geophysical Journal International* 203(2): 869–882. DOI: https://doi.org/10.1093/gji/ggv343.

HANSEN BT and WEMMER K, 2011, Age and evolution of the basement rocks in Thailand. In: Ridd MF, Barber AJ and Crow MJ (eds.), *The Geology of Thailand*. Geological Society of London.

KIL D, HONG TK, CHUNG D, KIM B, LEE J and PARK S, 2021, Ambient noise tomography of upper crustal structures and Quaternary faults in the Seoul metropolitan area and its geological implications. *Earth and Space Science* 8(11): 1-27. DOI: https://doi.org/10.1029/2021EA001983.

KOSUWAN S, TAKASHIMA I and CHARUSIRI P, 2018, Active Fault Zones in Thailand. Available at: http://www.dmr.go.th/main.php?filename=fault_en.

KOZAR MG, CRANDALL GF and HALL SE, 1992, Integrated Structural and Stratigraphic Study of the Khorat Basin, Rat Buri Limestone (Permian), Thailand. Paper presented at the National Conference on "Geologic Resources of Thailand: Potential for Future Development," Bangkok, Thailand, 17-24 November.

KREEMER C, BLEWITT G and KLEIN EC, 2014, A geodetic plate motion and global strain rate model. *Geochemistry, Geophysics, Geosystems* 15(10): 3849–3889. DOI: https://doi.org/10.1002/2014GC005407.

LASKE G, MASTERS G, MA Z and PASYANOS M, 2013, Update on CRUST1.0 - A 1-degree Global Model of Earth's Crust. EGU General Assembly 2013, held 7-12 April, 2013 in Vienna, Austria, id. EGU2013-2658, 15. Available at: http://adsabs.harvard.edu/abs/2013EGUGA..15.2658L.

LÉVÊQUE JJ, RIVERA L and WITTLINGER G, 1993, On the use of the checker-board test to assess the resolution of tomographic inversions. *Geophysical Journal International* 115(1): 313–318. DOI: https://doi.org/10.1111/j.1365-246X.1993.tb05605.x.

LEVSHIN AL and RITZWOLLER MH, 2001, Automated detection, extraction, and measurement of regional surface waves. *Pure and Applied Geophysics* 158(8): 1531–1545. DOI: https://doi.org/10.1007/PL00001233.

LIN FC, RITZWOLLER MH, TOWNEND J, BANNISTER S and SAVAGE MK, 2007, Ambient noise Rayleigh wave tomography of New Zealand. *Geophysical Journal International* 170(2): 649–666. DOI: https://doi.org/10.1111/j.1365-246X.2007.03414.x.

LIN YL, YEH MW, LEE TY, CHUNG SL, IIZUKA Y and CHARUSIRI P, 2013, First evidence of the Cambrian basement in Upper Peninsula of Thailand and its implication for crustal and tectonic evolution of the Sibumasu terrane. *Gondwana Research* 24(3-4): 1031–1037. DOI: https://doi.org/10.1016/j.gr.2013.05.014.

LOVATT SMITH PF, STOKES RB and BRISTOW C, 1996, Mid-Cretaceous inversion in the Northern Khorat Plateau of Lao PDR and Thailand. Geological Society, London, *Special Publications* 106(1): 233–247. DOI: https://doi.org/10.1144/GSL.SP.1996.106.01.15.

MORLEY CK, CHARUSIRI P and WATKINSON IM, 2011, Structural geology of Thailand during the Cenozoic. In: In: Ridd MF, Barber AJ and Crow MJ (eds.), *The Geology of Thailand*. Geological Society of London.

NOISAGOOL S, BOONCHAISUK S, PORNSOPIN P and SIRIPUNVARAPORN W, 2014, Thailand's crustal properties from tele-seismic receiver function studies. *Tectonophysics* 632: 64–75. DOI: https://doi.org/10.1016/j.tecto.2014.06.014.

NOISAGOOL S, BOONCHAISUK S, PORNSOPIN P and SIRIPUNVARAPORN W, 2016, The regional moment tensor of the 5 May 2014 Chiang Rai earthquake (Mw=6.5), Northern Thailand, with its aftershocks and its implication to the stress and the instability of the Phayao Fault Zone. *Journal of Asian Earth Sciences* 127: 231–245. DOI: https://doi.org/10.1016/j.jseaes.2016.06.008.

PANANONT P, HERMAN MW, PORNSOPIN P, FURLONG KP, HABANGKAEM S, WALDHAUSER F and WECHBUNTHUNG B, 2017, Seismotectonics of the 2014 Chiang Rai, Thailand, earthquake sequence. *Journal of Geophysical Research: Solid Earth* 122(8): 6367–6388. DOI: https://doi.org/10.1002/2017JB014085.

POVEDA E, JULIÀ J, SCHIMMEL M and PEREZ-GARCIA N, 2018, Upper and middle crustal velocity structure of the Colombian Andes from ambient noise tomography: Investigating subduction-related magmatism in the overriding plate. *Journal of Geophysical Research: Solid Earth* 123(2): 1459–1485. DOI: https://doi.org/10.1002/2017JB014688.

RIDD MF, BARBER AJ and CROW MJ, 2011, Introduction to the geology of Thailand. In: Ridd MF, Barber AJ and Crow MJ (eds.), The Geology of Thailand. Geological Society of London.

SAETANG K, 2017, Focal Mechanisms of Mw 6.3 Aftershocks from Waveform Inversions, Phayao Fault Zone, Northern Thailand. *International Journal of Geophysics* 2017: 9059825. DOI: https://doi.org/10.1155/2017/9059825.

SAETANG K, 2022, Two-layer model of anisotropy beneath Myanmar and Thailand revealed by shear-wave splitting.

Annals of Geophysics 65(6): 1–13. DOI: https://doi.org/10.4401/ag-8769.

SAETANG K and DURRAST H, 2023, A minimum 1-D velocity model of Northern Thailand. *Journal of Seismology* 27(3): 493-504. DOI: https://doi.org/10.1007/s10950-023-10148-6.

SAETANG K, SRISAWAT W and DURRAST H, 2018, Crustal Structures, Geothermal Sources and Pathways Beneath Northern Thailand Revealed by Local Earthquake Tomography. *Chiang Mai Journal of Science* 45(1): 565–575.

SEARLE MP and MORLEY CK, 2011, Tectonic and thermal evolution of Thailand in the regional context of SE Asia. In: Ridd MF, Barber AJ and Crow MJ (eds.), *The Geology of Thailand*. Geological Society of London.

SHAPIRO NM, CAMPILLO M, STEHLY L and RITZWOLLER MH, 2005, High-resolution surface-wave tomography from ambient seismic noise. *Science* 307(5715): 1615–1618. DOI: https://doi.org/10.1126/science.1108339.

SHIRZAD T and SHOMALI ZH, 2014, Shallow crustal structures of the Tehran basin in Iran resolved by ambient noise tomography. *Geophysical Journal International* 196(2): 1162–1176. DOI: https://doi.org/10.1093/gji/ggt449.

SIANGPIPOP S, 2022, Shear wave velocity model by c1 and c2 combination using ambient seismic noise beneath Northern Thailand. PhD Thesis. Graduate School, Chiang Mai University. Available at: http://cmuir.cmu.ac.th/jspui/handle/6653943832/78165.

STOKES RB, LOVATT SMITH PF and SOUMPHONPHAKDY K, 1996, Timing of the Shan-Thai-Indochina collision: new evidence from the Pak Lay Foldbelt of the Lao PDR. *Geological Society, London, Special Publications* 106(1): 225–232. DOI: https://doi.org/10.1144/GSL.SP.1996.106.01.14.

WANG YD, LIN FC, SCHMANDT B and FARRELL J, 2017, Ambient noise tomography across Mount St. Helens using a dense seismic array. *Journal of Geophysical Research: Solid Earth* 122(6): 4492–4508. DOI: https://doi.org/10.1002/2016JB013769.

YANG YJ, RITZWOLLER MH, LEVSHIN AL and SHAPIRO NM, 2007, Ambient noise Rayleigh wave tomography across Europe. *Geophysical Journal International* 168(1): 259–274. DOI: https://doi.org/10.1111/j.1365-246X.2006.03203.x.

Received 1 April 2025
Accepted 25 July 2025